Taylor & Francis
Taylor & Francis Group

Combustion Science and Technology

ISSN: (Print) (Online) Journal homepage: https://www.tandfonline.com/loi/gcst20

# A Shortcut Method to Predict Particle Size Changes during Char Combustion and Gasification under regime II Conditions

**Thobias Kreitzberg, Aekjuthon Phounglamcheik, Nils Erland L. Haugen, Reinhold Kneer & Kentaro Umeki**

**To cite this article:** Thobias Kreitzberg, Aekjuthon Phounglamcheik, Nils Erland L. Haugen, Reinhold Kneer & Kentaro Umeki (2022) A Shortcut Method to Predict Particle Size Changes during Char Combustion and Gasification under regime II Conditions, Combustion Science and Technology, 194:2, 272-291, DOI: 10.1080/00102202.2019.1678919

**To link to this article:** https://doi.org/10.1080/00102202.2019.1678919

COMBUSTION SCIENCE AND TECHNOLOGY
2022, VOL. 194, NO. 2, 272–291
https://doi.org/10.1080/00102202.2019.1678919

Taylor & Francis
Taylor & Francis Group



# A Shortcut Method to Predict Particle Size Changes during Char Combustion and Gasification under regime II Conditions

Thobias Kreitzberg[a], Aekjuthon Phounglamcheik[b], Nils Erland L. Haugen[c], Reinhold Kneer[a], and Kentaro Umeki[b]

[a]Institute of Heat and Mass Transfer, RWTH Aachen University, Aachen, Germany; [b]Energy Engineering, Div. Energy Science, Luleå University of Technology, Luleå, Sweden; [c]Department of Thermal Energy, SINTEF Energy Research, Trondheim, Norway

**ABSTRACT**

In most industrial applications, combustion and gasification of char progresses under regime II conditions. Unlike in other regimes, both particle size and density change simultaneously in regime II due to non-uniform consumption of carbon inside the particles. In this work, mathematical predictions of diameter changes in regime II were made by a one-dimensional simulation tool, where transient species balances are resolved locally inside the particle. This simulation is computationally expensive and usually not appropriate for the implementation in comprehensive CFD simulations of combustion or gasification processes. To overcome this restraint, an alternative shortcut method with affordable computation time has been developed and validated against the detailed model. This method allows the calculation of diameter changes during combustion and gasification from precalculated effectiveness factors. Additionally, the change of particle size has been investigated experimentally in a single particle converter setup. Therein, particles are fixed on a sample holder placed in the hot flue gas of a flat flame burner. Size and temperature trends are optically assessed by a 3CCD camera.

**ARTICLE HISTORY**
Received 8 February 2019
Revised 25 September 2019
Accepted 26 September 2019

**KEYWORDS**
combustion; gasification; char conversion; biomass; particle size change

## Introduction

Conversion of solid carbonaceous fuel particles in combustion or gasification applications is a complex multi-scale process influenced by a large variety of transport phenomena. Generally, the process can be subdivided into three sub-processes: evaporation of moisture, devolatilization and heterogeneous char conversion. In many cases, the last step mentioned is considered to be the slowest, therefore residence time needed for complete carbon conversion is predominantly controlled by heterogeneous char conversion. Consequently, precise knowledge about these reaction kinetics becomes mandatory for the design and dimensioning of technical apparatuses.

While there exists a vast number of studies focusing on the measurement of char reactivity (e.g. by thermogravimetric analysis), only a few studies investigate the change in particle size during char conversion. Subsequently, also the amount of available and validated model approaches is scarce. This is a problem, since an accurate prediction of

**CONTACT** Thobias Kreitzberg kreitzberg@wsa.rwth-aachen.de Institute of Heat and Mass Transfer, RWTH Aachen University, Augustinerbach 6, Aachen 52062, Germany

This article has been republished with minor changes. These changes do not impact the academic content of the article. Color versions of one or more of the figures in the article can be found online at www.tandfonline.com/gcst.

transient particle size progression during char conversion is important for the simulation of reactive particle-laden flows.

Depending on reaction conditions and fuel properties, different physical and chemical effects can dominate heterogeneous char conversion and play a rate-limiting role. In this context, three different regimes of fuel conversion can be distinguished: In regime I, the heterogeneous reaction of carbon itself represents the rate-limiting step. Here, mass transport processes like internal particle diffusion and external mass transfer are distinctly faster than the heterogeneous reaction. Hence, the reactions are regarded as the rate-limiting step while mass transfer effects can be completely neglected in modeling approaches. For this case, char conversion proceeds uniformly throughout the entire particle, because no gradients of reacting gas species evolve. As a result, the diameter stays constant during reaction until the particle is fully converted. In this regime, char density decreases linearly with conversion, which can be described by the so-called uniform reaction model (URM). This model is given by Eq. 1 in combination with dimensionless parameters $\alpha = 1$ and $\beta = 0$ (Mitchell 1989). In Eq. 1, $\rho_p$ is the apparent char density, $m_p$ the particle mass and $d_p$ the diameter. Generally speaking, $\alpha$ and $\beta$ are correlated through the equation $\alpha + 3\beta = 1$ for spherical particle shapes (Haugen, Tilghman, Mitchell 2014).

$$\frac{\rho_\mathrm{p}}{\rho_{\mathrm{p},0}} = \left(\frac{m_\mathrm{p}}{m_{\mathrm{p},0}}\right)^{\alpha} \quad \text{and} \quad \frac{d_\mathrm{p}}{d_{\mathrm{p},0}} = \left(\frac{m_\mathrm{p}}{m_{\mathrm{p},0}}\right)^{\beta} \tag{1}$$

In regime III, external mass transfer of gases from the bulk phase to the particle surface is the slowest and thus the rate limiting overall transport process. The reactions occur only at the external surface of the particle, resulting in an unaffected and constant particle density. The diameter on the other hand decreases continuously, which can be expressed by means of the shrinking core model (SCM). In this case, the dimensionless parameters become $\alpha = 0$ and $\beta = {}^1/_3$ for spheres and $\beta = {}^1/_2$ for infinitely long cylinders, respectively.

Lastly, regime II is dominated by the combination of both, reaction and intraparticle diffusion. Carbon consumption inside the particle is non-uniform, meaning that diameter as well as density change during conversion. For this reason, models predicting particle size changes under regime II require further input parameters or more computational effort than under regimes I and III. A model predicting particle size changes under regime II conditions is given by *Haugen et al.* (Haugen, Tilghman, Mitchell 2014), which has been validated by resolved particle simulations. In this model, particle radius $r_\mathrm{p}$ and density $\rho_\mathrm{p}$ changes are divided into two distinct phases, separated by the critical conversion $X_\mathrm{crit}$: During the initial stage of char conversion ($X \leq X_\mathrm{crit}$), the radius stays unaffected while the average density decreases proportionally to the change in particle mass (Eqs. 2–3):

$$\frac{\mathrm{d}r_\mathrm{p}}{\mathrm{d}t} = \begin{cases} 0 & \text{if } X \leq X_\mathrm{crit} \\ \frac{\mathrm{d}m_\mathrm{p}}{\mathrm{d}t}\frac{1-\eta}{4\pi r_\mathrm{p}^2 \rho_\mathrm{p}} & \text{if } X > X_\mathrm{crit} \end{cases} \tag{2}$$

$$\frac{\mathrm{d}\rho_\mathrm{p}}{\mathrm{d}t} = \begin{cases} \frac{\mathrm{d}m_\mathrm{p}}{\mathrm{d}t}\frac{1}{V_\mathrm{p}} & \text{if } X \leq X_\mathrm{crit} \\ \frac{\mathrm{d}m_\mathrm{p}}{\mathrm{d}t}\frac{\eta}{V_\mathrm{p}} & \text{if } X > X_\mathrm{crit} \end{cases} \tag{3}$$

In Eqs. 2 and 3, $V_p$ represents the particle volume and $\eta$ is the effectiveness factor. The particle radius starts to decrease at the beginning of phase two when $X > X_{crit}$, according to Eq. 2. By solving this set of equations it is possible to predict particle size and density changes numerically under regime II conditions. Since solving for $r_p$ and $\rho_p$ requires integration of time-dependent variables, it is later referred to as an "integral approach". An issue when applying this approach might be the precise determination of: *Haugen et al.* (Haugen, Tilghman, Mitchell 2014) offer two different methods to obtain the critical conversion. The first option involves a temporal integration of the reactions at the outer surface of the particle, which demands a spatially resolved particle simulation to calculate $\eta(t)$. The other option is a simplification where the critical conversion is approximated by the mean effectiveness factor ($X_{crit} \approx \bar{\eta}$).

The purpose of this study is to offer a predictive shortcut model that describes the change in particle size from common parameters used for expressing the intrinsic rate of char conversion. For this purpose, a one-dimensional detailed particle simulation model was set up, describing intraparticle transport phenomena and heterogeneous char gasification and combustion reactions. After validation with the in-situ experimental observation of particle size and surface temperature during char conversion, the one-dimensional model was used to validate a more simplified approach in predicting $X_{crit}$ that does not depend on local particle resolution. Since the particles are unresolved (i.e. 0D), the model can be applied for the calculation of a large number of particles simultaneously. Hence, the model allows burner simulations to be performed with more realistic physical predictions.

## Experimental investigation

### Charcoal preparation

Char samples were prepared from beech wood via pyrolysis in a screw reactor. The preparation was conducted at a reactor temperature of 773 K with a residence time of 5 min. A detailed description of the reactor and sample preparation can be found in (Morgano et al. 2015; Mueller et al. 2015). Proximate and ultimate analyses of the char sample are shown in Table 1.

The char particles were sieved to size fractions between 900 and 2000 µm. Prior to each experiment, the initial size of the char particles was measured by a light microscope. An example of a particle image taken through the microscope is depicted in Figure 1a.

### Experimental apparatus and procedure

The experimental investigation of char conversion was conducted in a single particle converter. Figure 1b shows a schematic diagram of the experimental setup. Major components are a McKenna type flat flame burner (Holthuis & Associates), an optical accessible reaction chamber, a 3CCD camera, and an LED blue light. Premixed combustion of $CH_4/O_2$-$CO_2$

**Table 1.** Proximate and ultimate analysis of the wood char sample (Mueller et al. 2015).

| Proximate Analysis | | | Ultimate Analysis (wt.-%,dry) | | | | |
|---|---|---|---|---|---|---|---|
| Water (wt.-%) | Volatiles (wt.-%,dry) | Ash (wt.-%,dry) | C | H | O | N | S |
| 3.6 | 23.3 | 3.1 | 81.2 | 3.3 | 12.1 | 0.3 | $\approx$ 0 |

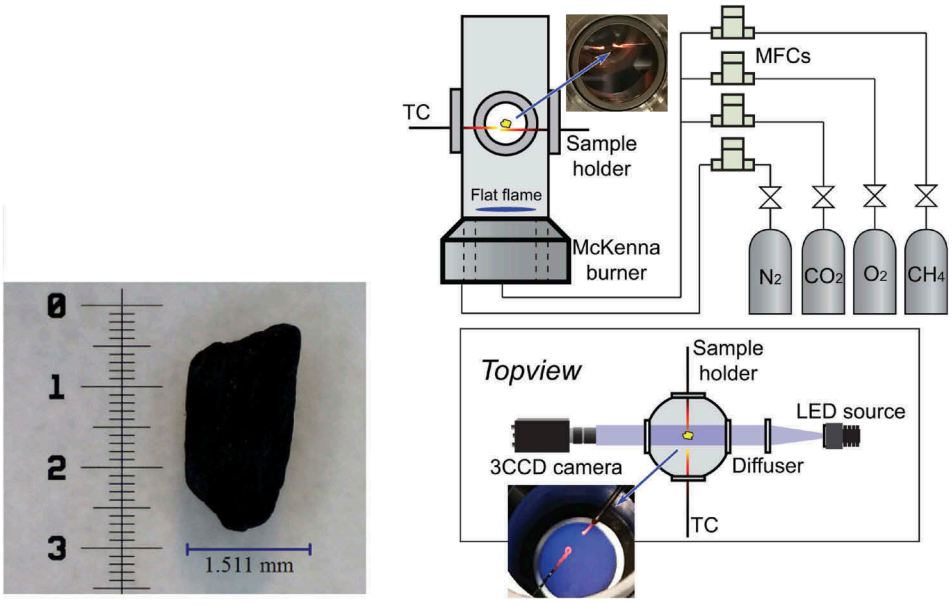


**Figure 1.** Example of a char particle (a) and schematic diagram of the experimental setup (b).

mixtures are utilized for heat supply to the reaction chamber. Thereby, the flat flame burner creates a well-defined temperature and gas composition distribution. Gas flow rates are regulated by mass flow controllers (El-Flow Select, Bronkhorst). Through ports of the reaction chamber, a particle holder, as well as an N-type thermocouple (model: NQXL-IM15G-300, Omega Ltd) with a diameter of 1.5 mm, are placed at the same height above the burner.

For each experiment, after the temperature reading from the thermocouple reached a stable value, a single char particle was inserted manually to the reaction chamber. The evolution of the char particle, as the conversion progresses, was recorded by a 3CCD camera (model: CV-M9GE, JAI Inc.), which holds three optically aligned independent sensors and dichroic prisms splitting incoming light based on wavelengths. A triple-band bandpass filter (Semrock) is installed in the camera to selectively transmit light at wavelengths between 446–468 nm, 520–540 nm, and 614–642 nm. Strong emission caused by persistent lines of inorganic elements (e.g. 589–590 nm by sodium and 404–405 nm, 766 and 770 nm by potassium) are eliminated by the filter. Therefore, only light emitted from the particle surface via thermal radiation is measured. A background of blue light is provided by an LED source through a light diffuser in the direction against the 3CCD camera. The obtained images were then processed to calculate the temporal changes in particle diameter and surface temperature.

Experiments were conducted with two different gas compositions in the converter, one being representative for combustion and one for gasification. These compositions were adjusted by gas flow rates of oxygen, methane and carbon dioxide, which are listed in Table 2.

**Table 2.** Gas composition and experimental conditions.

| | | Combustion | Gasification |
|---|---|---|---|
| **Gas flow rate** | | | |
| $CO_2$ | l $min^{-1}$ | 1.18 | 1.34 |
| $O_2$ | l $min^{-1}$ | 3.53 | 4.02 |
| $CH_4$ | l $min^{-1}$ | 1.18 | 2.01 |
| $N_2$ (ring) | l $min^{-1}$ | 5.79 | 7.24 |
| Gas velocity (at STD) | mm $s^{-1}$ | 200 | 250 |
| Air/fuel ratio ($\lambda$) | - | 1.5 | 1.0 |
| Gas temperature | K | 1275 | 1482 |
| **Gas composition**[a] | | | |
| $H_2O$ | - | 0.4 | 0.55 |
| $CO_2$ | - | 0.4 | 0.45 |
| $O_2$ | - | 0.2 | $\approx 0$ |

[a] calculated assuming equilibrium conditions, molar fraction.

## *Data analysis*

Due to radiative losses to the chamber wall, measurements of the thermocouple underestimate the temperatures of the surrounding gas. Therefore, measured values were corrected by using Eq. 4. Conductive heat losses to the supporting rod were neglected because of relatively uniform gas temperature in the radial direction.

$$T_g = T_{TC} + \frac{\sigma \epsilon_{TC} (T_{TC}^4 - T_w^4)}{h_q} \tag{4}$$

Here, $T_g$ and $T_{TC}$ are gas temperature and thermocouple reading, and $\sigma$ is the Stefan-Boltzmann constant. The wall temperature, $T_w$, was measured by an infrared thermometer (835-T2, testo). The emissivity, $\epsilon_{TC}$, is assumed to be 0.19, while the heat transfer coefficient $h_q$ is evaluated using a Nusselt number correlation for a cylinder in a cross flow, such that $Nu = 0.911 \cdot Re^{0.385} \cdot Pr^{0.4}$.

The images from the 3CCD camera were processed to obtain particle diameter and surface temperature. In order to isolate the particles within the images, the watershed

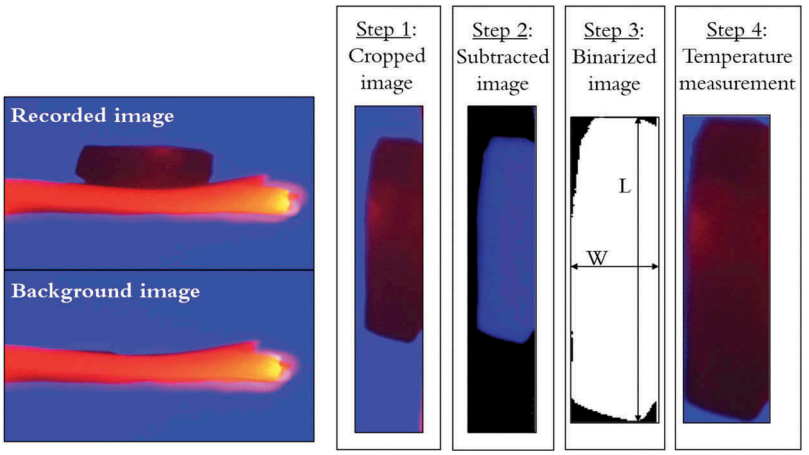


**Figure 2.** Image analysis procedure.

transformation was utilized. Figure 2 shows the image analysis procedure as conducted by watershed transformation: First, the original image was cropped manually to the particle area. Second, a background image was substracted from the cropped image, which only shows the particle holder. Afterward, the blue-color channel from the image was converted into grayscale, and then binarized. Finally, the particle area, length, and width of the particle were measured. An effective particle diameter is determined by $d = \sqrt{4\text{Area}/\pi}$, which will be used to represent particle diameter in the rest of this work. The surface temperature of the particle was estimated by two-color pyrometry using the red- and green-color channels from the images. Particularly for the surface temperature measurement, calibration of the 3CCD camera was done by acquiring images of a black body source between 1073 K and 1773 K with an interval of 100 K.

An initial decrease in particle size due to devolatilization during rapid heating was removed from the results in order to focus only on the period of the heterogeneous reactions. Data were collected until the particle diameter became constant, i.e. when the complete conversion was reached. The particle diameter and time were normalized as

$$d_{\text{p,norm}} = \frac{d_{\text{p}} - d_{\text{p,end}}}{d_{\text{p,0}} - d_{\text{p,end}}} \tag{5}$$

and

$$t_{\text{norm}} = \frac{t - t_{\text{end}}}{t_0 - t_{\text{end}}}, \tag{6}$$

respectively. In the above equations, $d_{\text{p}}$ and $t$ are particle diameter and time. The subscript norm, 0, and "end" represent normalized value, initial value, and final value.

## Modeling

The detailed one-dimensional model used in this work assumes a single perfectly spherical/cylindrical particle, radially discretized in evenly spaced shells with a thickness d$r$. Since a char particle is porous, each cell consists of a solid (carbonaceous) and a gaseous part. For each cell, an evolution equation is solved for the molar concentration of all gas phase species (cf. section 3.1). In this work, gases $CO_2$, CO, $H_2O$, $H_2$, and $O_2$ are considered. The heterogeneous reactions act as sources or sinks in this equation. In addition, evolution equations for occupied site fractions and the conversion of char are solved for the carbonaceous part (cf. section 3.2).

In the current approach, the solid is assumed to be in thermal equilibrium with the gas within the pores. Moreover, the conductive timescale of the particle is assumed to be very short compared to the chemical timescale, such that any thermal gradient within the particle can be neglected. Hence, there is no need to solve an energy equation for each shell within the particle. Instead, an evolution equation for energy, integrated over the entire particle, is solved in order to track its temperature evolution (cf. section 3.3). In the following, the above-mentioned equations will be explained, providing an overview of the overall model structure.

### Gas transport equation

The distribution of different gas species inside the particle is described by a transient transport equation taking multicomponent diffusion and heterogeneous surface reactions into account:

$$\frac{\partial C_\mathrm{i}}{\partial t} = \underbrace{\frac{1}{r^m}\frac{\partial}{\partial r}\left(r^m D_{\mathrm{eff,i}}\frac{\partial C_\mathrm{i}}{\partial r}\right)}_{J_\mathrm{i}} + \underbrace{S_\mathrm{g}\hat{\rho}_\mathrm{p}R_\mathrm{i}}_{\Phi_\mathrm{i}} \tag{7}$$

The three terms in this equation represent the temporal change of concentration $\frac{\partial C_\mathrm{i}}{\partial t}$, the diffusive flux $J_\mathrm{i}$ and a source/sink term $\Phi_\mathrm{i}$ due to heterogeneous reactions. $C_\mathrm{i}$ denotes the molar concentration of species i while $D_{\mathrm{eff,i}}$ is the effective diffusion coefficient of species i in a multicomponent gas mixture. The exponent $m$ becomes 2 for spherical and 1 for cylindrical particles. The mass-specific surface area $S_\mathrm{g}$ changes in each shell according to the random-pore model (Bhatia and Perlmutter 1981):

$$S_\mathrm{g} = S_{\mathrm{g},0}\cdot\sqrt{1-\psi\ln\left(1-\hat{X}\right)}. \tag{8}$$

Values for the initial surface area $S_{\mathrm{g},0}$ and the structural parameter $\psi$ can be found in Table A1. The local carbon density $\hat{\rho}_\mathrm{p}$ is directly proportional to the local carbon conversion $\hat{X}$ and can be expressed as:

$$\hat{\rho}_\mathrm{p} = \hat{\rho}_{\mathrm{p},0}\cdot\left(1-\hat{X}\right) \tag{9}$$

An approximation of the effective diffusion coefficients $D_{\mathrm{eff,i}}$ is obtained by the following expression (García-Camprubí, Sánchez-Insa, Fueyo 2010):

$$D_{\mathrm{eff,i}} = \frac{\epsilon}{\tau}\left(\sum_{\substack{j=1\\ j\neq i}}^{n}\frac{x_\mathrm{j}}{D_\mathrm{ij}} + \frac{1}{D_\mathrm{ik}}\right)^{-1} \tag{10}$$

By means of Eq. 10 the diffusion of species i through a porous matrix in a multicomponent gas mixture can be described. Therein, $\tau$ is the tortuosity and $x_\mathrm{j}$ is the molar fraction of gas i. Furthermore, $D_\mathrm{ij}$ are binary and $D_\mathrm{ik}$ are Knudsen diffusion coefficients. Their calculations are explained in the appendix by Eqs. 33 and 34. The particles' porosity $\epsilon$ can be determined from the local apparent particle density $\hat{\rho}_\mathrm{p}$ and the true carbon density $\rho_\mathrm{t}$, such that $\epsilon = 1-\hat{\rho}_\mathrm{p}/\rho_\mathrm{t}$ (Mitchell, Ma, Kim 2007).

To solve Eq. 7 numerically, boundary conditions at the particle center and at the outer surface must be provided. In consequence of assuming symmetric particles, at $r = 0$ the gas flux of each species is set to zero, leading to the first boundary condition (Eq. 11, I). At the outer surface, located at $r = d_\mathrm{p}(t)/2$, the diffusive flux of each gaseous species has to be equal to the external mass transfer, defined by the product of the mass transfer coefficient

$h_{m,i}$ and the concentration difference between the particle surface $C_{i,s}$ and the surrounding gas phase $C_{i,g}$ (Eq. 11, II).

$$\text{I}: \quad \left.\frac{\partial C_i}{\partial r}\right|_{r=0} = 0 \qquad \text{II}: \quad -D_{\text{eff},i}\left.\frac{\partial C_i}{\partial r}\right|_{r=d_p(t)2} = h_{m,i}\cdot\left(C_{i,s}-C_{i,g}\right) \tag{11}$$

The mass transfer coefficient $h_{m,i}$ is calculated according to Eq. 12 (Fatehi and Bai 2014):

$$h_{m,i} = \frac{\dot{m}/\rho_g}{\exp(\dot{m}/h_{m,i0}\rho_g)-1} \quad \text{with} \quad h_{m,i0} = \frac{\text{Sh}_i\cdot D_i}{d_p(t)} \tag{12}$$

where $\dot{m}$ is the mass flow per unit area leaving the particle, $\rho_g$ is the gas density, $\text{Sh}_i$ is the Sherwood number of species i and $D_i$ is the global diffusion coefficient of species i in the multicomponent gas mixture. For simplicity, the composition of the ambient gas is assumed to be constant in time. Since the particle shrinks as reaction proceeds, the location of the boundary condition at the particle surface is time-dependent. Beginning from $r = d_{p,0}/2$, the boundary moves toward the center of the particle until each shell is fully converted. Figure 3 visualizes the discretization scheme of the single particle and illustrates the different terms appearing in Eq. 7.

### Reaction mechanism

The applied model for the description of the heterogeneous gas-solid reactions is based on a simplified adsorption/desorption-mechanism. Therein, the assumption is made that the particle surface holds a finite number of total carbon sites per unit surface area, given by $\xi$. These sites can either be free ($C_f$) or form adsorbed C(O) complexes by reacting with $CO_2$, $H_2O$ or $O_2$. These three adsorption reactions are given by $R_1$, $R_2$ and $R_3$, respectively (cf. Table 3). The subsequent desorption of the carbon-oxygen complexes C(O) to gaseous CO is represented by $R_4$. Regarding $CO_2$ and $H_2O$ gasification reactions, the above-

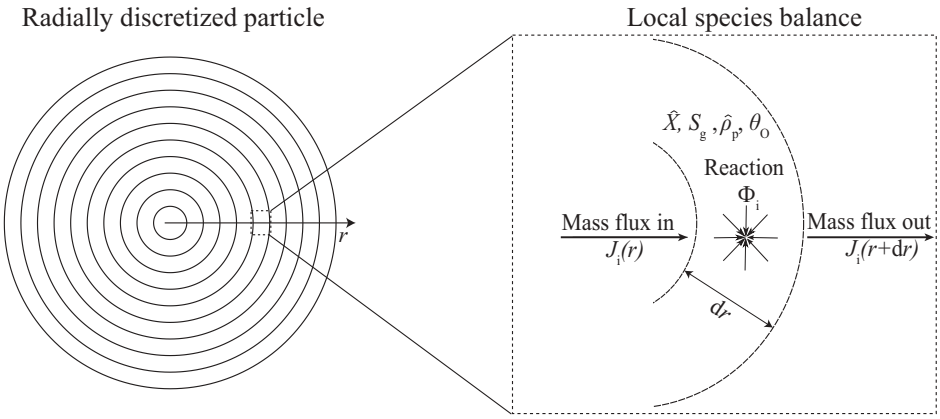


**Figure 3.** Discretization scheme and species balance of model approach.

**Table 3.** Reaction rate equations and enthalpies of reaction.

| Reaction equation | Rate equation [mol $m^{-2}s^{-1}$] | $\Delta H_j$ [kJ $mol^{-1}$] |
|---|---|---|
| $C_f + CO_2 \rightarrow C(O) + CO$ | $R_1 = \xi\, k_1\, \theta_f\, p_{CO_2}$ | 140 |
| $C_f + H_2O \rightarrow C(O) + H_2$ | $R_2 = \xi k_2\, \theta_f\, p_{H_2O}$ | 108 |
| $2C_f + O_2 \rightarrow C(O) + CO$ | $R_3 = \xi^2 k_3\, \theta_f^2\, p_{O_2}$ | −253 |
| $C(O) \rightarrow CO$ | $R_4 = \xi\, k_4\, \theta_O$ | 27.9 |

described adsorption/desorption mechanism is widely used in literature. However, it might be worth mentioning that reverse reactions of $R_1$ and $R_2$ are not considered in this work. The carbon-oxygen mechanism is strongly simplified and does not take the formation of $CO_2$ into account. Nevertheless, the work from *Tilghman et al.* showed that in the investigated range of temperature, the two reaction steps considered here might reflect the main route of the carbon-oxygen reaction (supplementary material in (Tilghman and Mitchell 2015)). The enthalpies of reaction are also taken from this work.

Rate constants are expressed by the Arrhenius equation $k_j = k_{0,j} \cdot \exp(-E_j/RT_p)$ to describe the temperature dependence of the reaction rates. The kinetic parameters (activation energy $E_j$ and pre-exponential factor $k_{0,j}$) used in this work have been determined by measurements in a fluidized bed reactor, which has been successfully used for the measurement of combustion (Gövert et al. 2017), gasification (Kreitzberg et al. 2016b) and pyrolysis (Pielsticker et al. 2019) kinetics, which are collected in Table A1. The fractional surface coverage of adsorbed carbon-oxygen complexes can be determined by means of Eq. 13 (Haugen, Mitchell, Tilghman 2015):

$$\frac{d\theta_O}{dt} = \frac{1}{\xi}(R_1 + R_2 + R_3 - R_4) + \theta_O A(R_3 + R_4) \tag{13}$$

In this expression, $A$ is a dimensionless variable defined by Eq. 32 in the appendix. As free ($\theta_f$) and occupied ($\theta_O$) surface site fractions have to sum up to 1 by definition, the amount of free active sites can be determined by $\theta_f = 1 - \theta_O$. (Haugen, Mitchell, Tilghman 2015; Mitchell, Ma, Kim 2007).

The local carbon conversion $\hat{X}$ is calculated in each shell, indicating the progress of reaction:

$$\frac{d\hat{X}}{dt} = S_g \cdot \left(1 - \hat{X}\right) \cdot M_c \cdot (R_3 + R_4) \tag{14}$$

Therein, $M_c$ is the molar mass of carbon. If conversion in the outer shell exceeds a predefined value of 99.9%, the layer is assumed to be fully converted, reducing the particle diameter $d_p$ by twice the layer thickness d$r$. The current particle diameter $d_p$ is calculated in each time step of the simulation to determine the present position of the boundary condition at the particle surface (Eq. 11).

## Energy balance

For calculation of the particle temperature, an energy balance is performed. Therein, heat transfer caused by convection of the surrounding gas ($\dot{Q}_{conv}$) and radiation between the

external surface of the particle and the walls of the reaction chamber ($\dot{Q}_{rad}$) are considered. Furthermore, the endo- and exothermicity of the heterogeneous reactions ($\dot{Q}_{reac}$) are included, leading to the following relation:

$$\frac{dQ_p}{dt} = \dot{Q}_{rad} + \dot{Q}_{conv} + \dot{Q}_{reac} \tag{15}$$

Therein, the particle's inner energy $Q_p$ is expressed by:

$$Q_p = m_{p,0}(1 - X)c_p T_p \tag{16}$$

Where $m_{p,0}$ represents the initial particle mass and $X$ is the global carbon conversion. The temperature dependence of the particle heat capacity $c_p$ is calculated by an approximation from *Merrick* (Merrick 1983). Radiative heat flux in Eq. 15 is implemented as:

$$\dot{Q}_{rad} = \sigma \epsilon_w A_p (T_p^4 - T_w^4) \tag{17}$$

Here, $\epsilon_w$ is the emissivity of the single-particle converter walls and is taken to be 0.4. The surface area available for convective and radiative heat transfer is given by $A_p = \pi d_p (L + {}^{d_p}/_2)$. In accordance with the experimental conditions, wall temperature differs for combustion ($T_w = 463$K) and gasification ($T_w = 528$K). The convective heat flux is defined as follows:

$$\dot{Q}_{conv} = h_q A_p (T_p - T_g) \tag{18}$$

In this expression, $T_g$ is the gas temperature, which is $T_g = 1273$K for combustion and $T_g = 1482$K for gasification conditions. $h_q$ is the heat transfer coefficient that is calculated analogously to the mass transfer coefficient (Fatehi and Bai 2014):

$$h_q = \frac{\dot{m} c_{p,g}}{\exp(\dot{m} c_{p,g} / h_{q,0}) - 1} \quad \text{with} \quad h_{q,0} = \frac{\mathrm{Nu} \cdot \lambda_g}{d_p(t)} \tag{19}$$

Therein, $\lambda_g$ and $c_{p,g}$ are thermal conductivity and isobaric heat capacity of the gas, respectively. Lastly, the heat sink or source caused by the heat of reaction is captured by:

$$\dot{Q}_{reac} = S_{tot} \sum_{j=1}^{n} R_j \Delta H_j \tag{20}$$

Where $S_{tot}$ represents the total surface area available for heterogeneous reactions, $R_j$ is the molar rate per surface area of reaction j and $\Delta H_j$ is its corresponding molar heat of reaction, listed in Table 3.

By discretization of the spatial derivatives in the gas transport equations (Eq. 7) with finite difference methods, a system of ordinary differential equations is obtained. This system, together with Eqs. 13, 14 and 15, is then numerically integrated with the help of the ode15s solver in Matlab®. Thereby, time and space-dependent values for $C_i, \theta_O$ and $\hat{X}$ are calculated.

## Results and discussion

### *Experimental results and comparison to 1d-simulation*

The experimental results reveal differences in the change of diameter for combustion and gasification conditions. Figure 4 shows measured diameters and temperatures of char particles under combustion condition. Particle diameters decrease progressively for the entire process as shown in Figure 4a. For the first part of the conversion process, the normalized rate of change of normalized particle diameter is higher for particles with larger initial diameters, $d_{p,0}$. In the case of larger particles, the particle size evolution moves toward the well-known shrinking core model . This result confirms that the combustion of large char particles progresses close to regime III, while smaller particles are reacting under regime II conditions. The particle surface temperature shown in Figure 4b during combustion indicates that the initial temperature of char particles is in the range of 1235–1300 K. The particle surface temperature increases due to exothermic reactions of char combustion, resulting in a maximum temperature in the range of 1274–1320 K at around the middle of the conversion. The missing temperature toward the end of conversion is due to the red and green light signals being too low when exothermic reactions are wearing off.

The changes of diameter and temperature of char particles under gasification conditions are shown in Figure 5. According to Figure 5a, the decrease in particle diameter is less pronounced during gasification than during combustion. Particle diameter stayed at above 90% of the initial diameter until normalized time of around 0.7–0.8, then the diameter started to shrink sharply. It is clearly visible that during char gasification the diameter followed neither the shrinking core model nor the uniform reaction model, which indicates regime II conditions. In addition, the particle temperature, as presented in

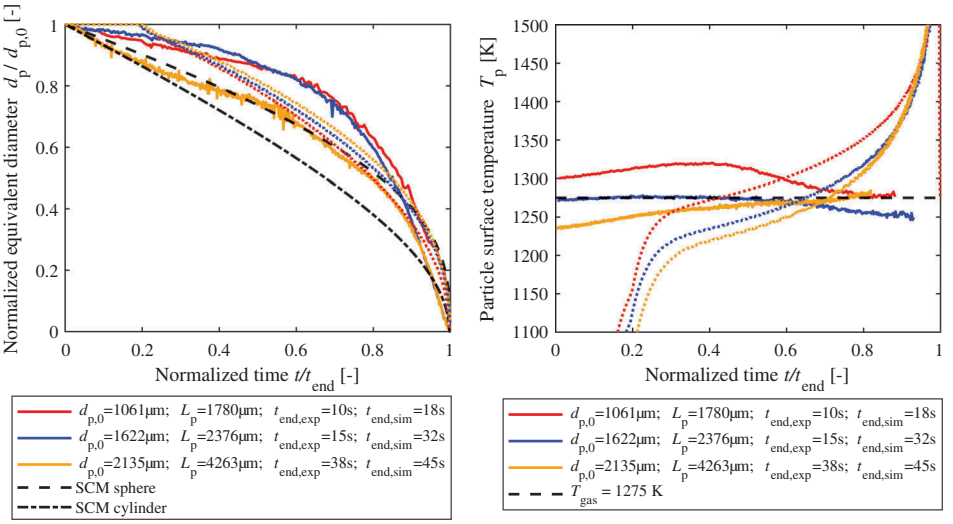


(a) Particle diameter (b) Particle surface temperature

Figure 4. Results obtained from experiments (solid lines) and 1D-simulations (dotted lines) for combustion conditions.

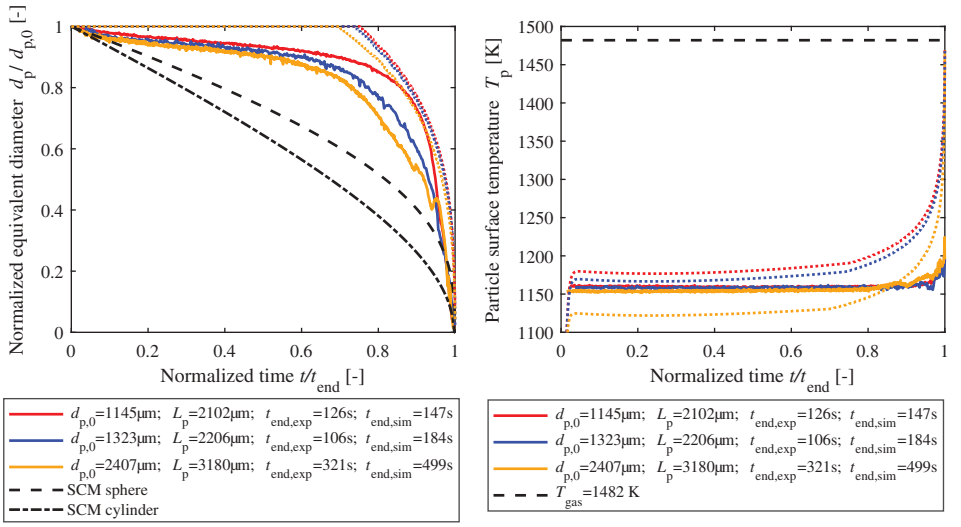


(a) Particle diameter (b) Particle surface temperature

**Figure 5.** Results obtained from experiments (solid lines) and 1D-simulations (dotted lines) for gasification conditions.

Figure 5b, was nearly constant at around 1160 K with a slight increase toward the end of the reaction.

Besides experimental findings, Figures 4 and 5 also show the results of the 1D-simulation. The boundary conditions and parameters used for the calculations can be found in Table A1 in the appendix. To approximate the shape of the biogenic char particles (cf. Figure 1a), simulations were carried out for cylinders. Results represent the experiments well with respect to the relationship between a normalized time and normalized diameter as well as particle surface temperature. However, there are a few discrepancies such as a slight decrease of particle diameter during the initial stage of conversion (cf. Figure 5a). This is most likely due to some physical effects not being described in 1D-simulation, such as local shrinkage. Furthermore, the reaction time spans show deviations for some cases, which might be due to the fact that gas atmospheres in the experimental setup are complex, including three different reacting gases for combustion conditions and two for gasification conditions. The kinetic parameters used for the simulations have been determined from experiments with only one reacting gas.

## *An analytical model for the change in particle size during char conversion*

With help of the model described in section 3, a parametric study examining the change of particle diameter during carbon conversion was conducted. Here, the change of particle size was investigated under isothermal conditions at $T_p = 1273$ K for spherical particles with different initial diameters $d_{p,0}$. The concentration of $CO_2$ in the surrounding gas was kept constant at a value of 20Vol.-% while the remaining 80Vol.-% consisted of $N_2$. Results are shown in Figure 6, where the normalized diameter is plotted over the global carbon conversion $X$. Additionally, two limiting cases, indicating regimes I (URM) & III (SCM) are included

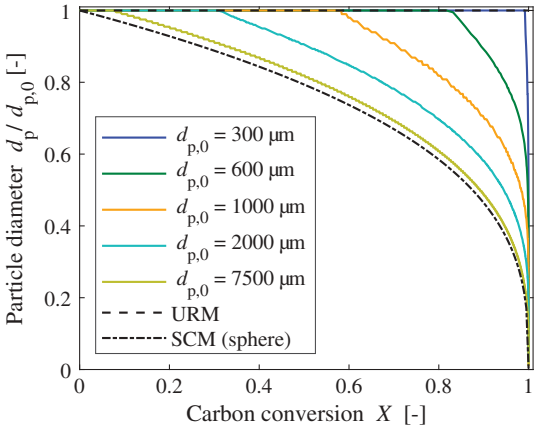


**Figure 6.** 1D-simulation results: change of normalized particle size over global conversion $X$ for different initial diameters $d_{p,0}$ and two limiting cases for regime I (URM) and regime III (SCM).

as dashed lines. As shown by the simulative results in this plot, the change in the size of char particles can be divided into two periods: During the initial period, the particle diameter stays constant until global conversion reaches a certain value (critical conversion $X_{crit}$), at which particles start shrinking. The smallest investigated particle size of $d_{p,0} =$ 300 µm reveals a constant size almost over the entire conversion process. Only when global conversion exceeds a critical value of $X_{crit} =$ 99%, a remarkable and steep decrease in diameter can be observed. For increasing initial particle sizes, the critical conversion $X_{crit}$ shifts toward smaller values, which means that particle shrinkage starts at earlier stages of conversion.

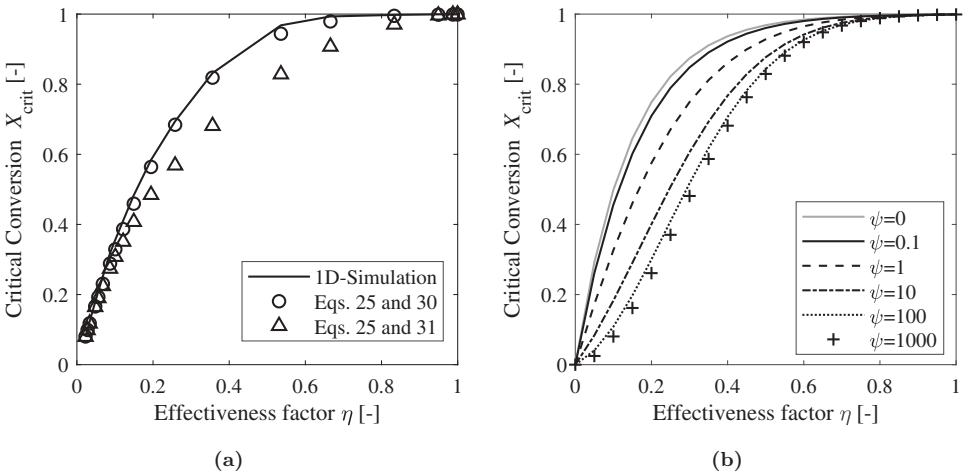


**Figure 7.** (a) Critical conversion $X_{crit}$ over effectiveness factor $\eta$: 1D-simulation (solid line) and presented method for predicting $X_{crit}$ from Eq. 25 (symbols) with two different options in calculating $\eta$ (Eqs. 30 and 31); (b) Effect of RPM parameter $\psi$ on critical conversion $X_{crit}$ in dependence of the effectiveness factors $\eta$, calculated with Eq 25.

Utilizing the obtained 1D-model results, the critical conversion is plotted over the effectiveness factor in Figure 7a (solid line). There, a non-linear relationship between the critical conversion and the effectiveness factor is revealed. This finding is inconsistent with the assumption made by *Haugen et al.* (Haugen, Tilghman, Mitchell 2014) ($X_{crit} \approx \bar{\eta}$), as stated in the introduction. Thus, this simplification cannot reproduce the evolution of the critical conversion accurately.

Therefore, this section describes the derivation of a simple expression for the determination of $X_{crit}$ by analyzing the relation between the progresses of global conversion $X$ and local conversion $\hat{X}$ at the outer surface of a particle.

During the initial stage, particle diameter stays constant, $d_p = d_{p,0}$, and the average particle density decreases with char conversion as $\rho_p = \rho_{p,0} \cdot (1 - X)$. Now, the critical conversion is defined as the global conversion at the moment when the char of the outermost shell of the particle is completely consumed. This study applied the random pore model (RPM), such that with the effectiveness factor, $\eta$, the overall and local conversion rates are given by:

$$\frac{dX}{dt} = \eta \cdot k_{RPM}(1 - X)\sqrt{1 - \psi \cdot \ln(1 - X)} \tag{21}$$

and

$$\frac{d\hat{X}}{dt} = k_{RPM}(1 - \hat{X})\sqrt{1 - \psi \cdot \ln(1 - \hat{X})}, \tag{22}$$

where $k_{RPM} = S_{g,0} \cdot (R_3 + R_4) \cdot M_c$. Integration of these equations from $t = 0$ to $t_{crit}$ (time to reach critical conversion) gives

$$\psi \cdot \eta \cdot k_{RPM} \cdot t_{crit} = \sqrt{1 - \psi \cdot \ln(1 - X_{crit})} - 1 \tag{23}$$

and

$$\psi \cdot k_{RPM} \cdot t_{crit} = \sqrt{1 - \psi \cdot \ln(1 - \hat{X}_{comp})} - 1, \tag{24}$$

where $\hat{X}_{comp}$ represents the predefined conversion when the local conversion is regarded to be completed ($\hat{X}_{comp} = 99.9\%$ in this study). By eliminating $t_{crit}$, the critical conversion is expressed as:

$$X_{crit} = 1 - \exp\left(-\frac{b\eta(b\eta + 2)}{\psi}\right), \text{where } b = \sqrt{1 - \psi \cdot \ln(1 - \hat{X}_{comp})} - 1. \tag{25}$$

Similarly, the critical conversion for $\psi = 0$ (i.e. no surface change due to pore growth/coalescence is considered) can be expressed as:

$$X_{crit} = 1 - \left(1 - \hat{X}_{comp}\right)^{\eta}. \tag{26}$$

After the critical conversion is reached, both density and particle diameter decrease with different proportion according to the effectiveness factor. With a similar approach of

*Haugen et al.* (Haugen, Tilghman, Mitchell 2014), the change in density after the critical conversion can be expressed as:

$$\frac{\rho_{\mathrm{p}}}{\rho_{\mathrm{p,0}}} = (1 - X_{\mathrm{crit}}) \cdot \left(\frac{1 - X}{1 - X_{\mathrm{crit}}}\right)^{\eta}. \tag{27}$$

From the relationship between particle mass, diameter, and the density, the change in particle diameter becomes:

$$\frac{d_{\mathrm{p}}}{d_{\mathrm{p,0}}} = \left(\frac{1 - X}{1 - X_{\mathrm{crit}}}\right)^{(1-\eta)/3}. \tag{28}$$

These expressions for density and particle diameter are the simplified form of the equations 2 and 3 under the assumption that the effectiveness factor is constant over the entire conversion. With such an assumption, the calculation of diameter changes is possible without the need for numerical integration. However, the errors could be non negligible when the effectiveness factor is prone to change significantly during conversion.

Figure 7a compares the critical conversion predicted by the 1D-simulation (as presented in section 3) with the critical conversion found from the newly developed approach (Eq. 25). The new model agrees well with the simulation results for low and high values of $\eta$ and reveals some deviations in the range of $0.3 < \eta < 0.7$. Figure 7a shows the impact of the effectiveness factor $\eta$ on the critical conversion $X_{\mathrm{crit}}$. Here, the effectiveness factors are calculated as follows:

$$\eta(t) = \frac{\text{Actual over all particle consumption rate}}{\text{Maximum over all particle consumption rate}} = \frac{\sum_{j=1}^{k} p_{\mathrm{CO_2,j}} \cdot \theta_{\mathrm{f,j}} \cdot S_{\mathrm{tot,j}}}{p_{\mathrm{CO_2,s}} \cdot \theta_{\mathrm{f,max}} \cdot S_{\mathrm{tot}}} \tag{29}$$

$$\bar{\eta} = \frac{1}{t_{\mathrm{end}}} \int_{t_0}^{t_{\mathrm{end}}} \eta(t)\, \mathrm{d}t \tag{30}$$

where $p_{\mathrm{CO_2,s}}$ is the partial pressure of $CO_2$ at the current particle surface and $S_{\mathrm{tot}}$ is the total particle surface area available for heterogeneous reactions. In addition, $p_{\mathrm{CO_2,j}}$, $\theta_{\mathrm{f,j}}$ and $S_{\mathrm{tot,j}}$ are the actual partial pressure, a fraction of free carbon sites and total surface area in shell j, respectively. It is obvious that Eq. 29 can only be solved when spatially resolved and transient information about the reactant gas partial pressure inside the particle is available. In other words, a potentially computationally costly particle resolved simulation as presented in this work has to be conducted a priori. The effectiveness factor calculated by means of Eq. 29 is time-dependent. To obtain an averaged value, Eq. 30 is utilized. An approach for the approximation of an averaged effectiveness factor $\bar{\eta}$ for adsorption/desorption reactions, solvable without knowledge about time and space-dependent reactant gas distributions, is given by *Hong et al.* (Hong, Hecker, Fletcher 2000):

$$\bar{\eta} = \frac{f}{\phi}\left(\frac{1}{\tanh(3\phi)} - \frac{1}{3\phi}\right) \tag{31}$$

with $\phi$ being the Thiele-modulus and $f$ a correction factor.

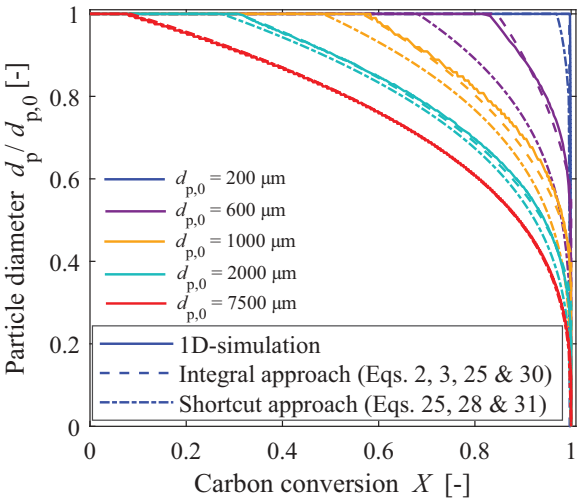


**Figure 8.** Predictions for the change of normalized particle size $d_p$ over global conversion $X$: 1D-simulation (solid lines), integral approach (dashed lines) and shortcut approach (chain lines).

Figure 7b also indicates that the critical conversion is not only affected by the effectiveness factor, but also by the parameter $\psi$ used for the random-pore model. Precisely, the critical conversion decreases with an increase in $\psi$.

In Figure 8 the change in particle size after critical conversion is plotted over global conversion. The lines are from 1D-simulation results and the newly developed approach in this work (Eq. 25). The model shows good agreement for small values of the effectiveness factor $\eta$. For large values of $\eta$ deviations occur, which are predominantly caused by the fact that predictions of $X_{crit}$ are less precise for larger $\eta$. The current model always underestimated simulation results, mainly because the model does not consider the change (i.e. increase) of the effectiveness factor during reactions.

The new model developed here is clearly more accurate than the simplified approach presented by *Haugen et al.* (Haugen, Tilghman, Mitchell 2014), and it should, therefore, be used for most cases. But, for situations where the effectiveness factor is known to change significantly before the critical conversion is reached, using the more expensive integral approach of *Haugen et al.* (Haugen, Tilghman, Mitchell 2014) will improve accuracy, since this approach does not rely on a constant effectiveness factor. Nevertheless, the shortcut approach developed in this work is useful for large-scale simulation involving a large number of particles as it provides reasonable prediction accuracy without numerical integration or prior 1D-simulation.

## Conclusion

An optical measurement system was applied for a single particle conversion reactor to simultaneously detect particle size and surface temperature under both gasification and combustion conditions. Regarding gasification experiments, char particles with a size of around 1 mm showed shrinkage behavior in regime II, i.e. distinct, but slower shrinkage than predicted by the shrinking core model . For combustion experiments, the diameter change behavior shifted from the one in regime II to the one in regime III, i.e. well

represented by the SCM, as the particle size increased. In terms of normalized time spans larger particles shrank faster, as expected by the size dependency of effectiveness factor.

Our 1D-simulation model could replicate the overall trend of the diameter changes despite the uncertainties in both model parameters, such as kinetic parameters, and the experimental conditions, e.g. gas temperature and complex particle morphology. However, room for improvement remains, such as the consideration of local shrinkage phenomena.

An analytical solution was obtained to describe the critical conversion, at which the particle starts shrinking, and the dependency of particle size reduction on the conversion after the critical conversion. The developed model showed a good agreement with the 1D-simulation model without introducing additional parameters. With improvement of the performance at high carbon conversion, $X > 0.9$, the model can potentially be implemented in large-scale simulation models.

## Acknowledgments

The authors would like to thank the German Research Foundation (DFG) for funding this work within the SFB/Transregio 129 ”Oxyflame” (project number 215035359). The authors also would like to thank Bio4Energy, Swedish Center for Biomass Gasification, Swedish Research Council and Kempe Foundation for the financial support. Nils Erland L. Haugen acknowledges the research project "Gaspro", financed by the Research Council of Norway (267916).

## Nomenclature

| | |
|---|---|
| $A$ | dimensionless parameter |
| $C$ | molar concentration |
| $c_p$ | heat capacity |
| $d$ | diameter |
| $D$ | diffusion coefficient |
| $E$ | activation energy |
| $h$ | heat or mass transfer coefficient |
| $\Delta H$ | Heat of reaction |
| $J$ | volumetric flux |
| $k$ | rate constant |
| $L$ | Length of particle |
| $m$ | mass |
| $\dot{m}$ | mass flow per unit area |
| $M$ | molar mass |
| $N_{av}$ | Avogadro constant |
| Nu | Nusselt number |
| $p$ | pressure |
| Pr | Prandtl number |
| Re | Reynolds number |
| $r$ | radius |
| $\sigma$ | Stefan-Boltzmann constant |
| $\sigma$ | average collision diameter |
| $\tau$ | tortuosity |
| $\phi$ | Thiele modulus |
| $R$ | reaction rate |
| $\Re$ | universal gas constant |
| $S$ | surface area |

| | |
|---|---|
| Sh | Sherwood number |
| $T$ | temperature |
| $t$ | time |
| $\hat{X}$ | local carbon conversion |
| $X$ | global carbon conversion |
| $x$ | molar fraction |
| $\alpha$ | dimensionless parameter |
| $\beta$ | dimensionless parameter |
| $\varepsilon$ | emissivity |
| $\varepsilon$ | particle porosity |
| $\eta$ | effectiveness factor |
| $\theta_O$ | fractional surface coverage of oxygen |
| $\theta_f$ | fractional free carbon sites |
| $\lambda$ | thermal conductivity |
| $\mu$ | dynamic viscosity |
| $\xi$ | surface concentration of C sites |
| $\rho$ | density |
| $\Phi$ | volumetric reaction rate |
| $\psi$ | structural parameter |
| $\Omega$ | collision integral |

## *Subscripts*

| | |
|---|---|
| 0 | initial |
| c | carbon |
| comp | completed reaction |
| conv | convection |
| crit | critical value |
| eff | effective |
| exp | experimental |
| g | gravimetric |
| g | gas |
| i | index variable: gases |
| j | index variable: reactions / shells |
| m | mass |
| m | exponent in differential equation |
| p | particle |
| q | heat |
| rad | radiation |
| reac | reaction |
| s | surface |
| t | true |
| TC | Thermocouple |
| tot | total |
| w | wall |

## References


Bhatia, S. K., and D. D. Perlmutter. 1981. A random pore model for fluid-solid reactions: II. diffusion and transport effects. *AIChE J.* 27 (2):247–54. doi:10.1002/(ISSN)1547-5905.

Bird, R., W. Stewart, and E. Lightfoot. 2006. *Transport phenomena*. New York..

Fatehi, H., and X. S. Bai. 2014. A comprehensive mathematical model for biomass combustion. *Combust. Sci. Technol.* 186 (4–5):574–93. doi:10.1080/00102202.2014.883255.

García-Camprubí, M., A. Sánchez-Insa, and N. Fueyo. 2010. Multimodal mass transfer in solid-oxide fuel-cells. *Chem. Eng. Sci.* 65 (5):1668–77. doi:10.1016/j.ces.2009.11.006.

Gövert, B. M., S. Pielsticker, T. Kreitzberg, M. Habermehl, O. Hatzfeld, and R. Kneer. 2017. Measurement of reaction rates for pulverized fuel combustion in air and oxyfuel atmosphere using a novel fluidized bed reactor setup. *Fuel* 201:81–92. doi:10.1016/j.fuel.2017.03.009.

Haugen, N. E. L., M. B. Tilghman, and R. Mitchell. 2014. The conversion mode of a porous carbon particle during oxidation and gasification. *Combust. Flame* 161 (2):612–19. doi:10.1016/j.combustflame.2013.09.012.

Haugen, N. E. L., R. Mitchell, and M. B. Tilghman. 2015. A comprehensive model for char particle conversion in environments containing $O_2$ and $CO_2$. *Combust. Flame* 162 (4):1455–63. doi:10.1016/j.combustflame.2014.11.015.

Hong, J., W. C. Hecker, and T. H. Fletcher. 2000. Improving the accuracy of predicting effectiveness factors for m th order and langmuir rate equations in spherical coordinates. *Energy Fuels* 14 (3):663–70. doi:10.1021/ef9902193.

Kreitzberg, T., B. M. Gövert, S. Pielsticker, and R. Kneer (2016a). $CO_2$ and $H_2O$ gasification under chemically and diffusion controlled conditions. In *33rd Annual International Pittsburgh Coal Conference*, Cape Town, South Africa.

Kreitzberg, T., H. D. Haustein, B. Gövert, and R. Kneer. 2016b. Investigation of gasification reaction of pulverized char under $N_2/CO_2$ atmosphere in a small-scale fluidized bed reactor. *J. Energy Res. Technol.* 138 (4):042207. doi:10.1115/1.4032791.

Merrick, D. 1983. Mathematical models of the thermal decomposition of coal2. Specific heats and heats of reaction. *Fuel* 62 (5):540–46. doi:10.1016/0016-2361(83)90223-5.

Mitchell, R., L. Ma, and B. Kim. 2007. On the burning behavior of pulverized coal chars. *Combust. Flame* 151 (3):426–36. doi:10.1016/j.combustflame.2007.07.014.

Mitchell, R. E. 1989. On the products of the heterogeneous oxidation reaction at the surfaces of burning coal char particles. *Symp. (Int.) Combust.* 22 (1):69–78. doi:10.1016/S0082-0784(89)80012-8.

Morgano, M. T., H. Leibold, F. Richter, and H. Seifert. 2015. Screw pyrolysis with integrated sequential hot gas filtration. *J. Anal. Appl. Pyrolysis.* 113:216–24. doi:10.1016/j.jaap.2014.12.019.

Mueller, A., H. D. Haustein, P. Stoesser, T. Kreitzberg, R. Kneer, and T. Kolb. 2015. Gasification kinetics of biomass- and fossil-based fuels: Comparison study using fluidized bed and thermogravimetric analysis. *Energy Fuels* 29 (10):6717–23. doi:10.1021/acs.energyfuels.5b01123.

Pielsticker, S., K. U. Schlögel, T. Kreitzberg, O. Hatzfeld, and R. Kneer. 2019. Biomass pyrolysis kinetics in a fluidized bed reactor: Measurements and plausibility verification for reaction conditions. *Fuel* 254:115589. doi:10.1016/j.fuel.2019.05.172.

Tilghman, M. B., and R. Mitchell. 2015. Coal and biomass char reactivities in gasification and combustion environments. *Combust. Flame* 162 (9):3220–35. doi:10.1016/j.combustflame.2015.05.009.

Wheeler, A., editor. 1951. *Reaction rates and selectivity in catalyst pores, volume 3 of advances in catalysis*. Elsevier.


## Appendix

Parameters and boundary conditions used in the 1D-simulations are collected in Table A1:

Calculation of the adsorbed surface complex C(O) is performed according to Eq. 13. Therein, the variable $A$ is expressed as Mitchell, Ma, and Kim (2007):

**Table A1.** Modeling parameters and boundary conditions.

| Condition | Unit | Combustion | Gasification | Parameter | Unit | Value |
|---|---|---|---|---|---|---|
| $T_g$ | K | 1275 | 1482 | $\rho_{p,0}$ | kg m$^{-3}$ | 680 |
| $T_w$ | K | 463 | 528 | $\rho_t$ | kg m$^{-3}$ | 2000 |
| $C_{CO_2,g}$ | mol m$^{-3}$ | 3.77 | 3.68 | $\tau$ | – | 3 |
| $C_{H_2O,g}$ | mol m$^{-3}$ | 3.77 | 4.42 | $S_{g,0}$ | m$^2$g$^{-1}$ | 6 |
| $C_{O_2,g}$ | mol m$^{-3}$ | 1.89 | 0 | $\epsilon_w$ | – | 0.4 |
| Nu | – | 2.18 | 1.80 | $\psi$ | – | 1 |
| $\lambda_g$ | W m$^{-1}$k$^{-1}$ | $9.79{\cdot}10^{-2}$ | $1.20{\cdot}10^{-1}$ | $d_{pore,0}$ | m | $13{\cdot}10^{-9}$ |
| $c_{p,g}$ | kJkg$^{-1}$K$^{-1}$ | 1.73 | 2.02 | $\xi$ | mol m$^{-2}$ | $1.08{\cdot}10^{-4}$ |
| $\rho_g$ | kgm$^{-3}$ | 0.298 | 0.245 | $k_{0,1}$ | s$^{-1}$Pa$^{-1}$ | $2.29{\cdot}10^{3}$ |
| $\mu_g$ | Pas | $5.02{\cdot}10^{-5}$ | $5.59{\cdot}10^{-5}$ | $k_{0,2}$ | s$^{-1}$Pa$^{-1}$ | $9.35{\cdot}10^{6}$ |
| | | | | $k_{0,3}$ | s$^{-1}$Pa$^{-1}$ | $4.63{\cdot}10^{8}$ |
| | | | | $k_{0,4}$ | s$^{-1}$ | $1.36{\cdot}10^{12}$ |
| | | | | $E_1$ | kJ mol$^{-1}$ | 253 |
| | | | | $E_2$ | kJ mol$^{-1}$ | 179 |
| | | | | $E_3$ | kJ mol$^{-1}$ | 128 |
| | | | | $E_4$ | kJ mol$^{-1}$ | 190 |

$$A = -\left(\frac{S_{g,0}^2}{S_g} \cdot \left(\frac{\psi}{2} - \frac{S_g^2}{S_{g,0}^2}\right)\right) \cdot M_c \tag{32}$$

Binary and Knudsen diffusion coefficients are determined by the following expressions:

$$D_{ij} = \frac{3}{16}\sqrt{\frac{2(\Re T)^3}{\pi}\left(\frac{1}{M_i} + \frac{1}{M_j}\right)}\frac{1}{N_{av} p \sigma_{ij}^2 \Omega_{ij}} \tag{33}$$

$$D_{ik} = \frac{d_{pore}}{3}\sqrt{\frac{8\Re T}{\pi M_i}} \tag{34}$$

Therein, $\Re$ is the universal gas constant, $M$ is the molar mass, $N_{av}$ is the Avogadro constant and $p$ is the pressure. Furthermore, $\sigma$ is the average collision diameter and $\Omega$ is the collision integral. Values thereof are taken from Bird, Stewart, and Lightfoot (2006).

The change of the pore diameter $d_{pore}$ is calculated according to Wheeler (1951):

$$d_{pore} = d_{pore,0} \cdot \frac{\epsilon}{\epsilon_0}\frac{\rho_t}{\hat{\rho}_c}\frac{S_{g,0}}{S_g} \tag{35}$$

Where $\epsilon$ is the particle porosity, $\rho_t$ and $\hat{\rho}_c$ are true and apparent (local) particle densities and $S_g$ is the gravimetric surface area. The initial pore diameter is $d_{pore,0} = 13$ for all calculations conducted in this work. This value has been approximated in Kreitzberg et al. (2016a).